



Quantitative assessment of various proxies for downscaling coarse-resolution VOD products over the contiguous United States

Shiyu Zhong, Lei Fan, Gabrielle de Lannoy, Frédéric Frappart, Jiangyuan Zeng, Mariette Vreugdenhil, Jian Peng, Xiangzhuo Liu, Zanpin Xing, Mengjia Wang, et al.

► To cite this version:

Shiyu Zhong, Lei Fan, Gabrielle de Lannoy, Frédéric Frappart, Jiangyuan Zeng, et al.. Quantitative assessment of various proxies for downscaling coarse-resolution VOD products over the contiguous United States. *International Journal of Applied Earth Observation and Geoinformation*, 2024, 130, pp.103910. 10.1016/j.jag.2024.103910 . hal-04618273

HAL Id: hal-04618273

<https://hal.inrae.fr/hal-04618273v1>

Submitted on 20 Jun 2024

HAL is a multi-disciplinary open access archive for the deposit and dissemination of scientific research documents, whether they are published or not. The documents may come from teaching and research institutions in France or abroad, or from public or private research centers.

L'archive ouverte pluridisciplinaire **HAL**, est destinée au dépôt et à la diffusion de documents scientifiques de niveau recherche, publiés ou non, émanant des établissements d'enseignement et de recherche français ou étrangers, des laboratoires publics ou privés.

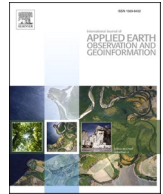


Distributed under a Creative Commons Attribution - NonCommercial - NoDerivatives 4.0
International License



Contents lists available at ScienceDirect

International Journal of Applied Earth Observation and Geoinformation

journal homepage: www.elsevier.com/locate/jag

Quantitative assessment of various proxies for downscaling coarse-resolution VOD products over the contiguous United States

Shiyu Zhong^{a,b}, Lei Fan^{a,b,*}, Gabrielle De Lannoy^c, Frédéric Frappart^d, Jiangyuan Zeng^e, Mariette Vreugdenhil^f, Jian Peng^{g,h}, Xiangzhuo Liu^d, Zanpin Xing^{d,i,j}, Mengjia Wang^k, Xiaojun Li^d, Huan Wang^{d,l}, Jean-Pierre Wigneron^d

^a Chongqing Jinpo Mountain Karst Ecosystem National Observation and Research Station, School of Geographical Sciences, Southwest University, Chongqing 400715, China

^b Chongqing Engineering Research Center for Remote Sensing Big Data Application, School of Geographical Sciences, Southwest University, Chongqing 400715, China

^c Department of Earth and Environmental Sciences, KU Leuven, B-3001 Heverlee, Belgium

^d INRAE, UMR1391 ISPA, Université de Bordeaux, Villenave d'Ornon F-33140, France

^e State Key Laboratory of Remote Sensing Science, Aerospace Information Research Institute, Chinese Academy of Sciences, Beijing 100101, China

^f Department of Geodesy and Geoinformation, Technische Universität Wien, 1040 Vienna, Austria

^g Department of Remote Sensing, Helmholtz Centre for Environmental Research-UFZ, Permoserstrasse 15, 04318 Leipzig, Germany

^h Remote Sensing Centre for Earth System Research, Leipzig University, Talstr. 35, 04103 Leipzig, Germany

ⁱ Cryosphere Research Station on the Qinghai-Tibet Plateau, State Key Laboratory of Cryospheric Science, Northwest Institute of Eco-Environment and Resource, Chinese Academy of Sciences, Lanzhou, Gansu 730000, China

^j University of Chinese Academy of Sciences, Beijing 100049, China

^k School of Geoscience and Technology, Zhengzhou University, Henan 450001, China

^l Institute of Ecology, College of Urban and Environmental Sciences, and Key Laboratory for Earth Surface Processes of the Ministry of Education, Peking University, Beijing 100871, China

ARTICLE INFO

Keywords:

Active microwave
Passive microwave
Vegetation optical depth (VOD)
Sentinel-1
Optical indices

ABSTRACT

Vegetation Optical Depth (VOD), a vegetation parameter that quantifies the extinction effect of microwaves penetrating the canopy, plays a crucial role in global-scale biomass monitoring and climate change research. However, the spatial gridding of existing long-term VOD products is relatively coarse (approximately 25 km), with restrictions on their application at a regional scale. High-resolution active-microwave proxies and optical vegetation indices can potentially be used to disaggregate coarse-resolution VOD, but it is unclear which proxy is optimal. In this paper, the Normalized Difference Vegetation Index (NDVI) and active-microwave proxies (VH, VV, and cross-polarization ratio CR) from Sentinel-1 were quantitatively assessed with VOD products at various frequencies (L-/C-/X-VOD) across the contiguous United States (U.S.). The results showed that VH ($R = 0.80$) and NDVI ($R = 0.77$) exhibit a high spatial correlation with L-VOD products. For temporal correlation, NDVI had the highest overall performances with all VOD products, but good correlations were also achieved with CR and, to a lesser extent, VH. Further comparisons of the performance between Brightness Temperature (TB) and VOD revealed that while TB displayed a strong temporal correlation with active-microwave proxies, its spatial correlations with such proxies were low. In contrast, VOD had good correlations both temporally and spatially with active-microwave proxies (e.g., VH). These evidences suggested that the downscaling of VOD using the combination of VH and other proxies could be an alternative promising method to estimate high-resolution VOD.

1. Introduction

Vegetation optical depth (VOD) is a variable parameterizing the microwave-based vegetation extinction effects (Frappart et al., 2020),

which has been potentially used to estimate vegetation water content (VWC) (Jackson and Schmugge, 1991), Gross Primary Production (GPP) (Teubner et al., 2018) and above-ground biomass (AGB) (Brandt et al., 2018; Cui et al., 2023; Fan et al., 2023, 2019; Tong et al., 2020; Vittucci

* Corresponding author at: Chongqing Jinpo Mountain Karst Ecosystem National Observation and Research Station, School of Geographical Sciences, Southwest University, Chongqing 400715, China.

E-mail address: leifan33@swu.edu.cn (L. Fan).

<https://doi.org/10.1016/j.jag.2024.103910>

Received 4 December 2023; Received in revised form 8 May 2024; Accepted 11 May 2024

Available online 16 May 2024

1569-8432/© 2024 The Authors. Published by Elsevier B.V. This is an open access article under the CC BY-NC-ND license (<http://creativecommons.org/licenses/by-nc-nd/4.0/>).

et al., 2019). Global long term VOD product datasets are available from various microwave sensors, e.g., C-band ASCAT (Advanced SCATterometer) (Liu et al., 2023, 2021) and C-band AMSR2 (Advanced Microwave Scanning Radiometer) (Owe et al., 2008), X-band AMSR2 (Karthikeyan et al., 2019; Wang et al., 2021a), and L-band SMOS (Soil Moisture and Ocean Salinity) (Wigneron et al., 2021) and SMAP (Soil moisture Active and Passive) (Chaubell et al., 2022; Konings et al., 2016).

Currently, the available VOD products are typically coarse (approximately 25 km) as they are generally retrieved from the brightness temperature (TB) measured by passive microwave sensors (e.g., SMOS and AMSR2) or backscatter data measured by scatterometers (e.g., ASCAT). The coarse resolution of these VOD products hampers their application to accurately monitor biomass dynamics and agroforestry management at regional scales. Those developed VOD products have coarse grid cells, hence each grid cell usually contains various land cover types, which leads to the limitation of monitoring the dynamic status of various vegetation classes (Vreugdenhil et al., 2020).

The vegetation information represented within the VOD products is different for the L-, C- or X-bands. Each channel has a different canopy sensing depth. Higher frequency (e.g., C-/X-band) VOD products are influenced by leaf properties, particularly leaf biomass, leaf area index, and leaf water potential (Momen et al., 2017; Olivares-Cabello et al., 2023; Schmidt et al., 2023). Compared to C-/X-band VOD, the low-frequency VOD at L-band is less influenced by leaf properties, enables deeper penetration into vegetation and soil, and is more sensitive to overall above-ground biomass (Chaparro et al., 2019; Rodríguez-Fernández et al., 2018; Schmidt et al., 2023).

The downscaling of coarse-resolution VOD products to high-resolution VOD will allow to obtain a high spatial resolution information of the VWC and AGB (Mohite et al., 2022). More importantly, high-resolution VOD products could potentially fill the gap that optical vegetation indices are only available under clear-sky conditions, enabling all-weather monitoring of vegetation dynamics at a fine scale. Previous studies (Das et al., 2019, 2014) have proposed a downscaling technique that is disaggregating the radiometer-based TB using high-resolution Synthetic Aperture Radar (SAR) backscatter data and subsequent inversion to target parameters. However, this method requires the high-resolution ancillary data such as land surface temperature (Fan et al., 2022; Peng et al., 2017). Alternatively, multiple data fusion downscaling methods in the framework of spatio-temporal machine learning may be a promising way to obtain high-resolution VOD, which could be performed using the relationships between optical or active-microwave proxies and VOD products.

Backscatter data in VV and VH polarization with high spatial (~20 m) and temporal (6–12 days) resolutions can be provided from the Sentinel-1 constellation (Torres et al., 2012). Sentinel-1 is a constellation of satellites launched by the European Space Agency (ESA) equipped with the C-band SAR. Disaggregating coarse-resolution VOD using high-resolution backscatter data could be prospective, but the implementation of these disaggregation methods is challenged by the different relationship between VOD and backscatter data, depending on different vegetation properties (Rötzer et al., 2017). It is because the backscatter of vegetated surfaces is related to VOD, but is also affected by soil backscatter and by the ratio between backscatter and extinction cross-sections of vegetation elements (Attema and Ulaby, 1978).

In previous studies, backscatter data, such as co-pol VV and cross-pol VH or HV, have been found to closely correlate with vegetation information monitored by VOD (El Hajj et al., 2019; Rötzer et al., 2017; Vreugdenhil et al., 2020; Zhou et al., 2022). For instance, Aquarius/SAC-D HV-pol backscatter data were used to retrieve L-band VOD (Rötzer et al., 2017), and recent studies used Sentinel-1 VV-pol backscatter to retrieve high-resolution (1-km) C-band VOD over agricultural areas (El Hajj et al., 2019) and grasslands (Zhou et al., 2022). Another proxy, the cross-polarization ratio (CR, calculated by the difference of VH- and VV-pol backscatter (in dB)) was found to be closely associated

with VWC (Vreugdenhil et al., 2018) and with optical vegetation indices (e.g., the normalized difference vegetation index, NDVI) (Veloso et al., 2017). Furthermore, Vreugdenhil et al., (2020) found high correlations between the temporal dynamics of Sentinel-1 CR and active microwave VOD from ASCAT and passive microwave VOD Climate Archive (VODCA, (Moesinger et al., 2020)) over Europe. Here, low correlations between VODCA and CR were found over sparse vegetation and deciduous forests. These studies show that the correlations between these active-microwave proxies (e.g., VV, VH, CR) and VOD can be variable, depending on vegetation types and regional factors.

Alternatively, optical vegetation indices with a high spatio-temporal resolution can serve as proxies to downscale coarse-resolution VOD. NDVI has a good spatio-temporal correlation with VOD at different frequencies (Lawrence et al., 2014; Li et al., 2021; Rodríguez-Fernández et al., 2018). However, the relationship between VOD and NDVI has rarely been compared to that between VOD and active-microwave proxies.

This research is aimed at determining the optimal high-resolution proxies for the downscaling coarse-resolution VOD at different frequencies. We are trying to comprehensively compare the relationship between VOD and these proxies at different frequencies, which is important for the development of downscaling algorithms. Thus, this study quantitatively assessed the performance of an optical index (i.e., NDVI) and Sentinel-1 based active-microwave proxies (i.e., VV, VH, and CR) to monitor the vegetation dynamics as observed in L-VOD from SMOS (Wigneron et al., 2021), C-/X-VOD_{AMSR2} from AMSR2 (Wang et al., 2021a) and C-VOD_{ASCAT} from ASCAT (Liu et al., 2023) across the contiguous United States (U.S.).

2. Datasets

2.1. Study region and land cover product

The contiguous U.S. (CONUS) was selected as the study region, and its vegetation types were shown in Fig. 1. In the contiguous U.S., there are different climate regimes and vegetation types, and Sentinel-1 backscatter observations have a revisit time of 6–12 days there. Therefore, the contiguous U.S. is a suitable test area to identify the optimal proxies for downscaling VOD products.

We use the 2020 ESA CCI LC (Climate Change Initiative Land Cover) to map the land cover over the contiguous U.S., which is a worldwide land cover dataset available with a grid-resolution of 300 m (ESA, 2017). There were 37 original LC classes in the ESA CCI LC product, which were merged into four classes, i.e., forest, shrubland, cropland and grassland (Fig. 1), following the rules given in Table S1 and excluding non-vegetation types. The 0.25° land cover map was produced from aggregating the 300 m map of four classifications (i.e., forest, shrubland, cropland and grassland) into a 0.25° map using dominant class inside every VOD grid cell.

2.2. VOD products

Four VOD datasets (referred to as VODs in the following) have been used in the assessment as listed in Table 1, including passive microwave-based SMOS L-VOD (Wigneron et al., 2021) and C-/X-VOD_{AMSR2} (Wang et al., 2021a), and active microwave-based C-VOD_{ASCAT} (Liu et al., 2023).

2.2.1. L-VOD

The L-VOD was acquired from the SMOS satellite based on the SMOS-IC algorithm (Wigneron et al., 2021). Daily global L-VOD were produced from SMOS descending and ascending orbits at 25 km grid resolution for 2010–2021 (Fan et al., 2023). Signals received by satellite sensors may be distorted due to radio frequency interference (RFI), leading to an unreliable VOD retrieval. L-VOD observations influenced by RFI are filtered out using the technique reported by Wigneron et al., (2021),

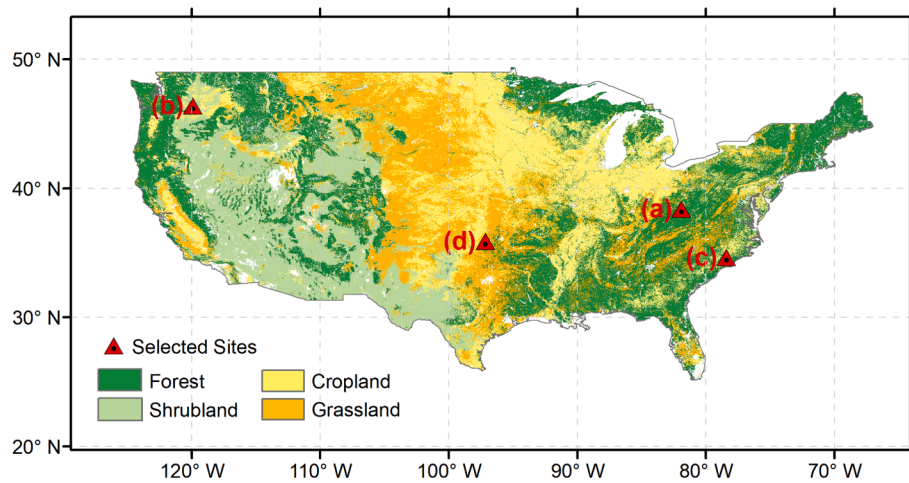


Fig. 1. The land cover classes for 2020 in the contiguous U.S. based on CCI LC product at 300 m spatial resolution. The land cover classes were merged into four classes (i.e., forest, shrubland, cropland, and grassland). The red points in the figure represent the four selected sites (pixels) to characterize the temporal variation of VOD and Sentinel-1 based active-microwave proxies in various vegetation conditions. (For interpretation of the references to colour in this figure legend, the reader is referred to the web version of this article.)

Table 1

Overview of utilized VOD datasets in the research.

Variable name	Sensor	Frequency	Period	Grid resolution	Temporal resolution	Reference
L-VOD	SMOS	1.4 GHz	01/2017–12/2020	25 km	Daily	Wigneron et al., (2021)
C-VOD _{ASCAT}	ASCAT	5.255 GHz	01/2017–12/2020	0.25°	Daily	Liu et al., (2023)
C-VOD _{AMSR2}	AMSR2	6.925 GHz	01/2017–12/2020	0.25°	Daily	Wang et al., (2021a)
X-VOD _{AMSR2}		10.65 GHz				

with a threshold on the root mean square error between the measured and simulated brightness temperature (referred to as TB-RMSE) equal to 8 K. In addition, L-VOD was reprojected and aggregated to 0.25° spatial resolution using bilinear interpolation, which was commonly employed in previous studies involving VOD processing (Chaparro et al., 2019; Li et al., 2021; Liu et al., 2018). Daily L-VOD from four years (2017–2020) were used in this study.

2.2.2. X-/C-VOD_{AMSR2}

The AMSR2 is a passive microwave sensor that provides accurate measurements of surface radiation through seven frequency channels. Wang et al., (2021a) provided daily X-VOD_{AMSR2} and C-VOD_{AMSR2} products at 0.25° resolution, which were derived from X-band (10.65 GHz) and C-band (6.925 GHz) AMSR2 TB observations (Wang et al., 2021a, 2021b). The X-/C-VOD_{AMSR2} products were retrieved from TB observations of the descending orbits, considering the heat balance in the soil, vegetation canopy, and near-surface air at night (Owe et al., 2008). The high-quality daily X-/C-VOD_{AMSR2} from 2017 to 2020 was obtained by filtering out retrievals using the technique reported by Wang et al., (2021a), with a threshold on TB-RMSE larger than 5 K.

2.2.3. C-VOD_{ASCAT}

The ASCAT scatterometer is a C-band sensor working at 5.255 GHz providing VV-pol backscatter observations at angles of incidence from 25° to 65° (Wagner et al., 2013). ASCAT can achieve a complete global coverage of the Earth in three days. Liu et al., (2023) developed a global C-band ASCAT IB VOD product (referred to as C-VOD_{ASCAT} in our study), which was retrieved with a multi-time (MT) based algorithm. The following study was conducted using daily C-VOD_{ASCAT} with 0.25° grid-resolution from 2017 to 2020.

2.3. TB Products from SMOS and AMSR2

The daily SMOS L3 TB product (referred to as SMOS TB in the

following), obtained from Centre Aval de Traitement des Données (CATDS), corresponds to the TB observations measured at multiple-angles and dual-polarization (i.e., horizontal and vertical, denoted as TB_H and TB_V, respectively) (Al Bitar et al., 2017). The CATDS L3 processor averages the SMOS TB observations with an angle bin width of 5° and bin centers ranging from 2.5° to 62.5°, which also includes an interpolation field at $\theta = 40^\circ$. In this study, only TB layers acquired during the ascending orbits from 2017 to 2020 were used (Li et al., 2022).

AMSR2 has a sun-synchronous orbit with an incidence angle of 55 degrees and provides TB observations at H-polarization (TB_H) and V-polarization (TB_V). We collected the TB (Level 3) from the AMSR2 (referred to as AMSR2 TB below) at C-band (6.925 GHz) (https://suzaku.eorc.jaxa.jp/GCOM_W/data/data_w_index.html). AMSR2 TB at the descending pass (1:30 am LST) was considered for four years from 2017 to 2020 in our study.

2.4. Sentinel-1 data

Sentinel-1 constellation is composed of two ESA-launched satellites, Sentinel-1A and Sentinel-1B (Torres et al., 2012). The two satellites provide Ground Range Detected (GRD) Interferometric Wide-swath (IW) backscattering coefficients (referred to as σ^0) in VV (σ_{VV}^0) and VH (σ_{VH}^0) polarization (Geudtner et al., 2014). The revisit period of two sensors (A and B) is 6 ~ 12 days (note that Sentinel-1B has not been operative since December 23, 2021, resulting in a revisit of ≥ 12 days with only one satellite). VV- and VH-pol backscattering coefficients from the ascending orbit during 2017–2020 were selected.

To obtain the high-quality Sentinel-1 backscatters, the pre-processing was as follows:

(1) Pre-processing of Sentinel-1 data.

The backscattering coefficients in VV and VH polarization were preprocessed using the Sentinel-1 Toolbox (S1TBX) supplied with Google Earth Engine, including the removal of thermal and GRD boundary

noise, radiometric correction, and ranging-Doppler topographic correction (Filipponi, 2019). Note that radar incidence angle has a significant impact on the observed backscattering coefficients. To reduce its effect, the cosine correction technique proposed by Ulaby et al., (1982) was used to normalize the Sentinel-1 data:

$$\sigma_{\theta_{ref}}^0 = \sigma_{\theta}^0 \times \frac{\cos^2 \theta_{ref}}{\cos^2 \theta} \quad (1)$$

where θ_{ref} is the reference incidence angle; θ is the local incidence angle; $\sigma_{\theta_{ref}}^0$ means the normalized backscattering coefficient; and σ_{θ}^0 represents the measured backscatter at corresponding local incidence angle. θ_{ref} was set as 40° of acquired Sentinel-1 data, thus the backscattering coefficients from different local incidence angle were normalized at 40° in this study. Finally, the normalized backscattering coefficients were transformed into dB by $10 \cdot \log_{10} \sigma^0$.

(2) Data selection

Low and high thresholds were applied to backscattering coefficients to minimize the effect of outliers with extremely higher or lower values, typically inconsistent with responses from vegetated areas. These outliers are often caused by noise from water bodies, buildings, and shaded areas. Based on the filter, the high-quality VV- and VH-pol backscattering coefficients were obtained in the range of $-20 \text{ dB} \leq \sigma_{VV}^0 \leq -5 \text{ dB}$ and $-26 \text{ dB} \leq \sigma_{VH}^0 \leq -11 \text{ dB}$, respectively (Bauer-Marschallinger et al., 2019). The spatial resolution of the VV- and VH-pol backscattering coefficients was resampled to 0.25° using the arithmetic mean for spatial matching with the VOD data.

2.5. MODIS NDVI product

The optical vegetation index NDVI was compared with each VOD product. The NDVI dataset was obtained from the Moderate-resolution Imaging Spectroradiometer (MODIS) Collection 6 NDVI products (MOD13A2 Collection 6; 16-day composites at a 1 km grid cell) for 2017–2020 (Didan, 2015). High-quality NDVI retrievals can be identified by referencing the quality control (QC) layer. NDVI was subsequently aggregated to 0.25° using nearest-neighbor interpolation.

3. Methods

3.1. The cross-polarization ratio (CR)

Sentinel-1 CR is calculated by the difference between VH- and VV-pol backscattering coefficients in the following form:

$$\sigma_{CR}^0 = \sigma_{VH}^0 - \sigma_{VV}^0 \quad (2)$$

where σ_{VH}^0 and σ_{VV}^0 are the backscattering coefficients in dB. CR is scarcely influenced by the variations of surface soil moisture (Khabbaza et al., 2022; Vreugdenhil et al., 2018), which makes it a useful indicator for monitoring crops (Jiao et al., 2009; Kim et al., 2012).

3.2. Spatial and temporal analysis

(1) Spatial analysis.

The relationships between proxies (VV, VH, CR, and NDVI) and VODs were estimated by comparing the average values of each dataset for the year of 2020. We conducted the Kolmogorov-Smirnov test at the $p < 0.05$ significance level and found that our datasets do not adhere to the assumption of a normal distribution. Therefore, the Spearman correlation coefficient (R) was used here to estimate the correlations between proxies and VODs (Vachaud et al., 1985). The Spearman correlation coefficient is a non-parametric measure that assesses the strength and direction of monotonic relationships between variables, and it does not assume that the variables are normally distributed (Hauke and Kossowski, 2011). It assesses the monotonic relationship

between the rank values of two variables. The expression for R is given by:

$$R = \frac{\sum_{i=1}^N (XY) - N(\frac{N+1}{2})^2}{N(N^2 - 1)/12} \quad (3)$$

where N represents sample size, and $(N + 1)/2$ denotes the average rank of X and Y , which stand for the proxies (i.e., VV, VH, CR, and NDVI) (X) and VODs (Y), respectively. It was regarded to be statistically significant R if $p < 0.05$.

(2) Temporal analysis.

Initially, to evaluate the relationships between all proxies (active-microwave proxies and NDVI) and VODs, VODs and active-microwave proxies for each pixel were averaged over 16 days for consistency with the temporal sampling of NDVI. The per-pixel temporal correlation between VODs and proxies was quantified by the Spearman correlation coefficient (R). Only significant R ($p < 0.05$) was used in the analysis.

Secondly, to assess of the correlation between active-microwave proxies and VODs, VODs were matched to the revisit period of Sentinel-1, which is 6 ~ 12 days. The temporal resolution of VOD products from SMOS, AMSR2, and ASCAT ranges from 1 to 3 days. Hence, the values of each VOD product were matched with the observations of Sentinel-1. Additionally, a half-width window of 6 days was employed to retrieve VOD observations that were temporally closest to the Sentinel-1 observations. Only grid points with a minimum of 60 paired observations during the period from 2017 to 2020 were utilized.

4. Results

4.1. Spatial pattern comparison

4.1.1. Across all land cover types

The spatial patterns of VODs (i.e., L-VOD, C-/X-VOD_{AMSR2}, and C-VOD_{ASCAT}) and proxies (i.e., VV, VH, CR, and NDVI) showed that L-VOD (Fig. 2a) and C-VOD_{ASCAT} (Fig. 2d) had similar spatial features. The highest VOD values were found in forest in the southeastern U.S., while areas with short vegetation in the central region generally exhibited lower VOD values. Notably, although C-/X-VOD_{AMSR2} (Fig. 2b, c) is generally higher relative to L-VOD (Fig. 2a) in grassland and cropland areas, their spatial patterns were similar to that of L-VOD. Considering active-microwave proxies, the spatial distributions of VV (Fig. 2e) and VH (Fig. 2f) were more related to vegetation classes (Fig. 1) relative to CR (Fig. 2g).

The corresponding density scatter plots and correlation coefficients between proxies and VODs for the year 2020 revealed a clear non-linear relationship (Fig. 3). Note that the correlations between VODs and NDVI ($R = 0.59$ – 0.77) were slightly higher than those between VODs and active-microwave proxies ($R = 0.46$ – 0.80). Specifically, L-VOD and C-VOD_{ASCAT} had the highest correlation with NDVI ($R = 0.77$, Fig. 3a, m), followed by C-VOD_{AMSR2} ($R = 0.74$, Fig. 3i) and X-VOD_{AMSR2} ($R = 0.59$, Fig. 3e), respectively.

In addition, strong spatial correspondence was found between L-VOD and active-microwave proxies, with R reaching 0.80 for VH (Fig. 3b), 0.75 for CR (Fig. 3c), and 0.73 for VV (Fig. 3d), respectively. Conversely, poor spatial correlations between active-microwave proxies and C-/X-VOD_{AMSR2} could be observed, as indicated by R values between VV and X-VOD_{AMSR2} lower than 0.5 (Fig. 3h).

4.1.2. Different land cover types

The median value of R between VODs and all proxies across the years (2017–2020) over different vegetation types were summarized (Fig. 4). The density scatter plots for 2020 and for different vegetation types were given in supplement figures (Fig. S1–S4).

Over forest, all correlations between VODs and proxies were lower than 0.5 (the 1st column in Fig. 4). L-VOD had the slightly higher correlation with all the proxies, relative to C-VOD_{ASCAT}, C-VOD_{AMSR2}, and

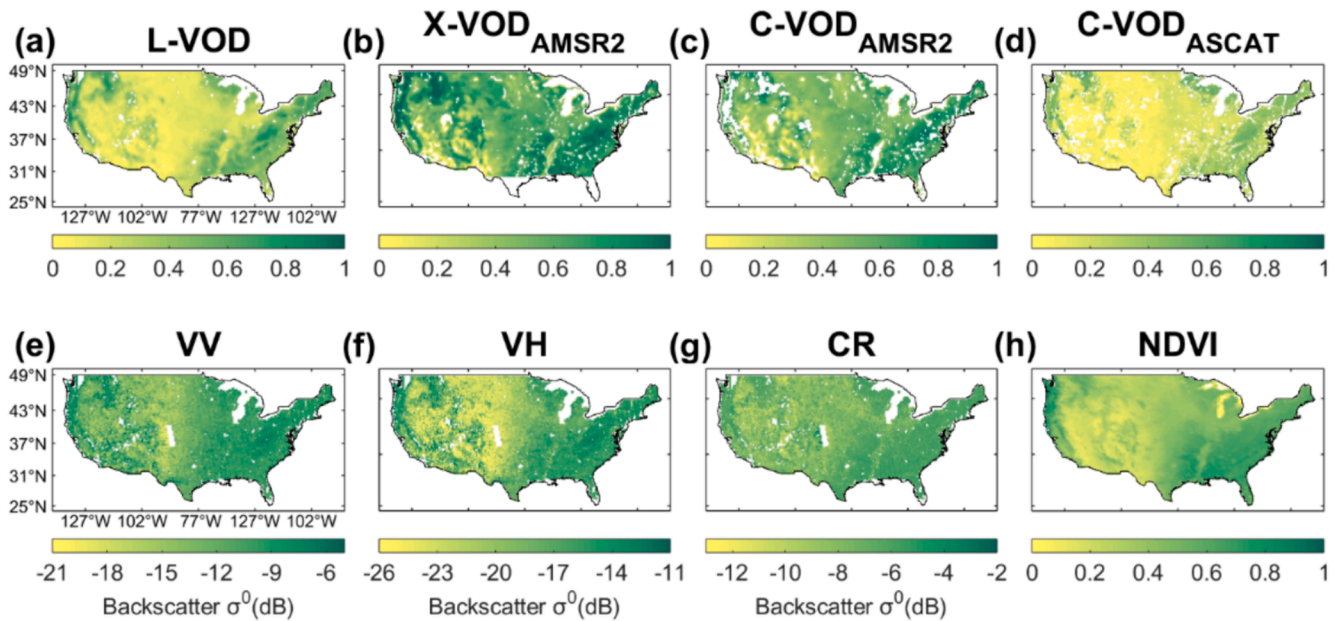


Fig. 2. Yearly VODs and proxies for 2020. Average of VODs for (a) L-VOD, (b) X-VOD_{AMSR2}, (c) C-VOD_{AMSR2}, (d) C-VOD_{ASCAT}, average of active-microwave proxies for (e) VV, (f) VH, (g) CR, and (h) average of NDVI.

X-VOD_{AMSR2}. For example, L-VOD showed the highest correlation with VV ($R = 0.35$, Fig. 4a), followed by C-VOD_{ASCAT} ($R = 0.32$, Fig. 4a), C-VOD_{AMSR2} ($R = 0.27$, Fig. 4a), and X-VOD_{AMSR2} ($R = 0.16$, Fig. 4a). Notably, active-microwave proxies saturated significantly compared with L-VOD (Fig. S1b–d). Similar saturation could be observed in the comparison of active-microwave proxies with the other three VODs (Fig. S1), indicating saturation of C-band active-microwave proxies over forest. Additionally, similar saturation could be observed in shrubland (Fig. S2), where correlations between active-microwave proxies and VODs were generally lower than 0.45 (the 2nd column in Fig. 4). Moreover, higher R values were observed in cropland, relative to forest and shrubland.

Over grassland, high correlations were generally observed between active-microwave proxies and VODs. Relative to VV (Fig. 4a) and CR (Fig. 4c), VH exhibited the highest correlations with VODs, with R of 0.82 for L-VOD, 0.75 for C-VOD_{ASCAT}, 0.70 for C-VOD_{AMSR2}, and 0.45 for X-VOD_{AMSR2} (Fig. 4b).

In comparison to active-microwave proxies (Fig. 4a–c), NDVI exhibited superior performance over forest, shrubland, cropland and grassland (Fig. 4d). For example, correlations between NDVI and C-VOD_{AMSR2} reached 0.41 over forest, 0.61 over shrubland, 0.58 over cropland, and 0.72 over grassland (Fig. 4d).

4.2. Temporal correlation between proxies and VODs

Per-pixel temporal correlations between 16-day averaged VOD products and proxies were shown in Fig. 5. Overall, the correlation distributions of L-VOD with VV, VH, and CR were found to be spatially similar (Fig. 5a, e, i). Positive correlations could be observed in the central U.S., which was covered by grassland or cropland. A distinct positive relationship existed in the Mississippi River Basin in the south-central U.S., mainly covered by cropland. On the contrary, negative correlations between L-VOD and active-microwave proxies could be observed in most shrubland and forest areas. Specifically, the correlations between L-VOD and active-microwave proxies were negative over eastern forest and most shrubland, while they were positive over western forest, cropland and grassland (Fig. 5a, e, i). Notably, the negative relationship between L-VOD and NDVI could be observed only in the western U.S. (Fig. 5m).

Similar patterns (the distribution of R values between active-

microwave proxies and L-VOD) could be observed in X-VOD_{AMSR2} (Fig. 5b, f, j) and C-VOD_{AMSR2} (Fig. 5c, g, k). Compared with NDVI, X-VOD_{AMSR2} (Fig. 5n) and C-VOD_{AMSR2} (Fig. 5o) presented positive R values over 93 % and 95 % of the pixels, respectively. In the western U. S., a few negative correlations (less than 10 % of the pixels) could be seen between NDVI and C-/X-VOD_{AMSR2}. Note that the active microwave VOD product (C-VOD_{ASCAT}) was positively correlated with either VV or VH over most of the study area, while the passive VOD products (L-VOD, C-VOD_{AMSR2}, and X-VOD_{AMSR2}) exhibited negative correlation with either VV or VH ($R < 0$) in southeastern and western U.S.

The strongest per-pixel correlations between active-microwave proxies and VODs were shown in Fig. 6. Pixels with an absolute difference in R values below 0.02 were shaded in gray. The comparison was based on the daily temporal correlations between active-microwave proxies and VODs, which were shown in Supplementary Fig. S5. The percentages of pixels exhibiting the highest R values for every active-microwave proxy were given in the rectangular box within each sub-graph in Fig. 6.

Overall, CR was better correlated with passive VODs, relative to VV or VH over most of the study area (Fig. 6a–c). In Fig. 6a, CR had the highest correlation with L-VOD over 36.76 % of the pixels, followed by VH (23.12 %) and VV (17.46 %). A similar pattern for the highest R could be observed for C-/X-VOD_{AMSR2} (Fig. 6b, c). For C-/X-VOD_{AMSR2}, the highest correlations were generally found for CR (over 50.06 % and 44.95 % of the pixels, respectively), showing highest R values in the central and eastern U.S. Note that VV (33.86 %) and VH (31.71 %) performed better with active microwave-based C-VOD_{ASCAT}, relative to CR (13.72 %) (Fig. 6d).

To account for the seasonality of the active-microwave proxies and VODs, a time series analysis was conducted, based on daily L-VOD and active-microwave proxies at four selected sites (see Fig. 1). Fig. 7 showed the time series of active-microwave proxies and L-VOD for four vegetation types, i.e., (a) forest, (b) shrubland, (c) cropland and (d) grassland. Over forest and shrubland (Fig. 7a, b), contrasting temporal trends were apparent between L-VOD and active-microwave proxies. For example, over forest (Fig. 7a), L-VOD showed an increase from March to June and a slight decrease in October and November. Simultaneously to the increase of L-VOD, CR and VH decreased, resulting in negative correlation coefficients of -0.76 and -0.79 (Fig. 7a), respectively. Consistent temporal variations were found between active-

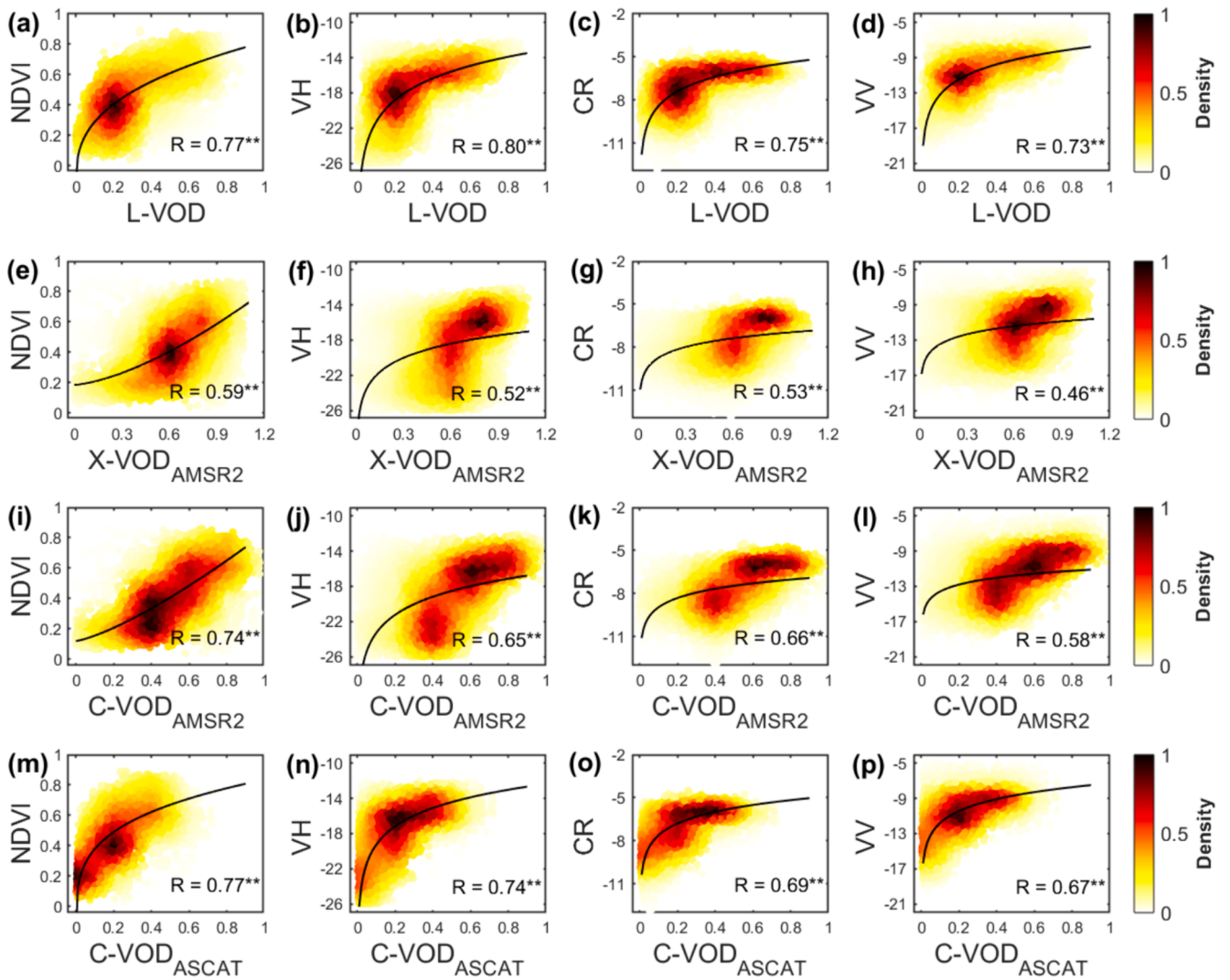


Fig. 3. Density scatter plots between average L-VOD (1st row), X-VOD_{AMSR2} (2nd row), C-VOD_{AMSR2} (3rd row), C-VOD_{ASCAT} (4th row) and NDVI (1st column), VH (2nd column), CR (3rd column), VV (4th column) for 2020. Note that ** denotes significant correlation with the 0.05/0.01 confidence level ($p < 0.05/0.01$).

microwave proxies and L-VOD at sites covered by mild vegetation, i.e., the cropland (Fig. 7c) and the grassland (Fig. 7d). Generally, for sites in cropland and grassland, L-VOD and active-microwave proxies increased with vegetation growth and decreased during senescence. Over the grassland site (Fig. 7d), the seasonal dynamics of active-microwave proxies and L-VOD were closely consistent (e.g., R values for CR and L-VOD was 0.89).

4.3. Comparison of the spatio-temporal performance of TBs and VODs

Note that the available passive VOD products are retrieved from the TB measured by passive microwave sensors. Moreover, VOD was retrieved using the difference between TB_V and TB_H ($TB_V - TB_H$) (Owe et al., 2001). Previous studies have proposed a method to retrieve high-resolution passive microwave-derived products (e.g., VOD and soil moisture) by downscaling TB using high-resolution radar backscattering coefficient (Das et al., 2019, 2014). This method is based on the assumption that TB has a close relationship with radar backscattering coefficient. Thus, to better explore the potential downscaling VOD methods, we made the comparison of the correlations between coarse-resolution VODs and radar backscattering coefficients vs. the correlations between coarse-resolution TB datasets (TB_V , TB_H and $TB_V - TB_H$) and radar backscattering coefficients. Here, coarse-resolution TB

datasets and VODs from SMOS and AMSR2 were compared with active-microwave proxies from Sentinel-1 (i.e., VV, VH and CR).

At the spatial scale, the spatial correlations of the active-microwave proxies with TB datasets ($|R| < 0.6$, Fig. S6, S7) were found to be lower than the ones achieved with VODs (Fig. 3). At the temporal scale, the per-pixel temporal correlations between TB datasets and active-microwave proxies (Fig. S8, S9) were comparable to that between VOD and active-microwave proxies (Fig. S5). Notably, the temporal dynamics of TB_H and TB_V are similar, indicated by almost the same distribution pattern of temporal correlations between active-microwave proxies and either TB_H or TB_V (e.g., Fig. S8a and Fig. S8b). However, the spatial pattern of temporal correlations between active-microwave proxies and $TB_V - TB_H$ appears to differ. For example, the negative correlation pixels between CR and either AMSR2 TB_H (Fig. S8g) or AMSR2 TB_V (Fig. S8h) could be observed in the southeast U.S. covered by forest, where CR was positively correlated with AMSR2 $TB_V - TB_H$ (Fig. S8i).

For C-band, AMSR2 TB_H (TB_V , Fig. S10c) showed the best performance with CR (Fig. 8c), reaching 4,285 pixels, followed by VH (2541 pixels, Fig. 8b) and VV (2388 pixels, Fig. 8a). There were more highly correlated pixels between AMSR2 TB_H (TB_V , Fig. S10a–c) and active-microwave proxies, compared to the correlations between C-VOD_{AMSR2} and active-microwave proxies (Fig. 8a–c). Therefore, downscaling of TB using active-microwave proxies is a superior option for

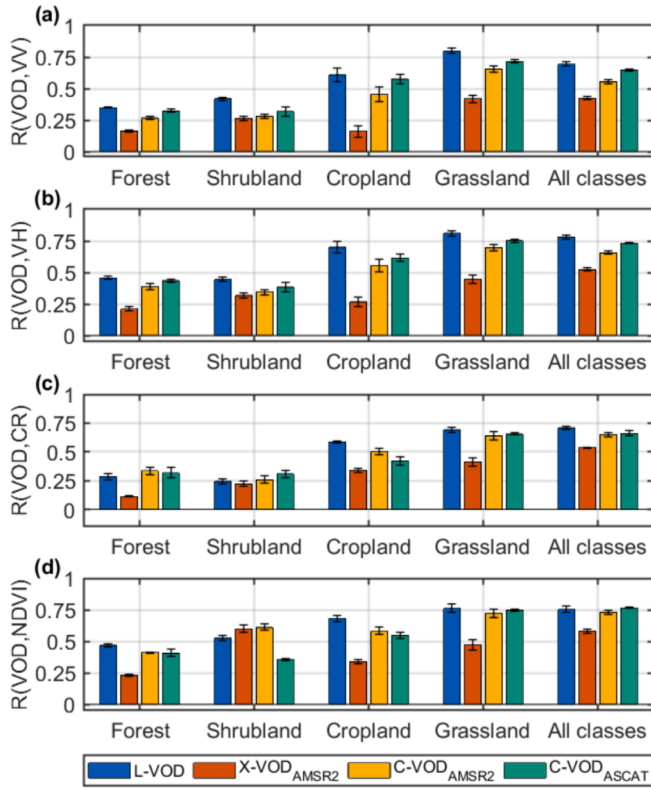


Fig. 4. Comparison of median value of R for the spatial correlation for each vegetation class during 2017–2020 between yearly average VODs and (a) VV, (b) VH, (c) CR, and (d) NDVI (error bars represent the standard deviation (std)).

retrieving high-resolution VOD products from C-band. Similarly, for L-band, SMOS TB_H (TB_V , Fig. S10f) also showed the best performance with CR (4220 pixels, Fig. 8f). Note that more highly correlated pixels can be observed between SMOS L-VOD and VH (3070 pixels), relative to the

correlations between SMOS TB_H (TB_V , Fig. S10e) and VH (2077 pixels, Fig. 8e). VH was also found to have a better correlation with L-VOD relative to TB_V - TB_H (Fig. S11e). These evidences suggested that VH is more appropriate for downscaling L-VOD products, relative to down-scale TB datasets from L-band.

5. Discussion

5.1. Performance of spatial correlations

Our results showed generally a positively and non-linear spatial relationship between high-resolution proxies and VODs in the contiguous U.S. It can be directly explained by the positive difference between the backscattering coefficient of developed vegetation and the one of soil, particularly at VH polarization. Therefore, an increase of vegetation biomass (or height or density) is associated to an increase of active-microwave proxies, besides the obvious increase of VOD products and NDVI. This is true for VH and, to a lesser extent, for VV. In addition, the good correlation between VH and VOD could be attributed to the fact that the backscattering coefficient has a positive correlation with the permittivity of the object, so backscattering coefficient generally rises with increasing vegetation moisture content (indicated by VOD) (McNairn and Shang, 2016).

The saturation effect of active-microwave proxies over high-density vegetation should be noted, although there are good spatial correlations between proxies and VODs. Specifically, our results showed that active-microwave proxies saturated slightly while the VODs still increase (Fig. 3). This saturation, which was also reported in previous studies, poses limitations to the use of backscattering coefficient as a tool to monitor biomass, particularly at the higher frequencies (Imhoff, 1995; Joshi et al., 2017). The empirical correlations between AGB and backscatter observations had corroborated the different degrees of saturation in the C-, L- and P-band (Imhoff, 1995). A possible explanation for the saturation is the increase in canopy cover, especially in late growth and decurrent forms (Lucas et al., 2006).

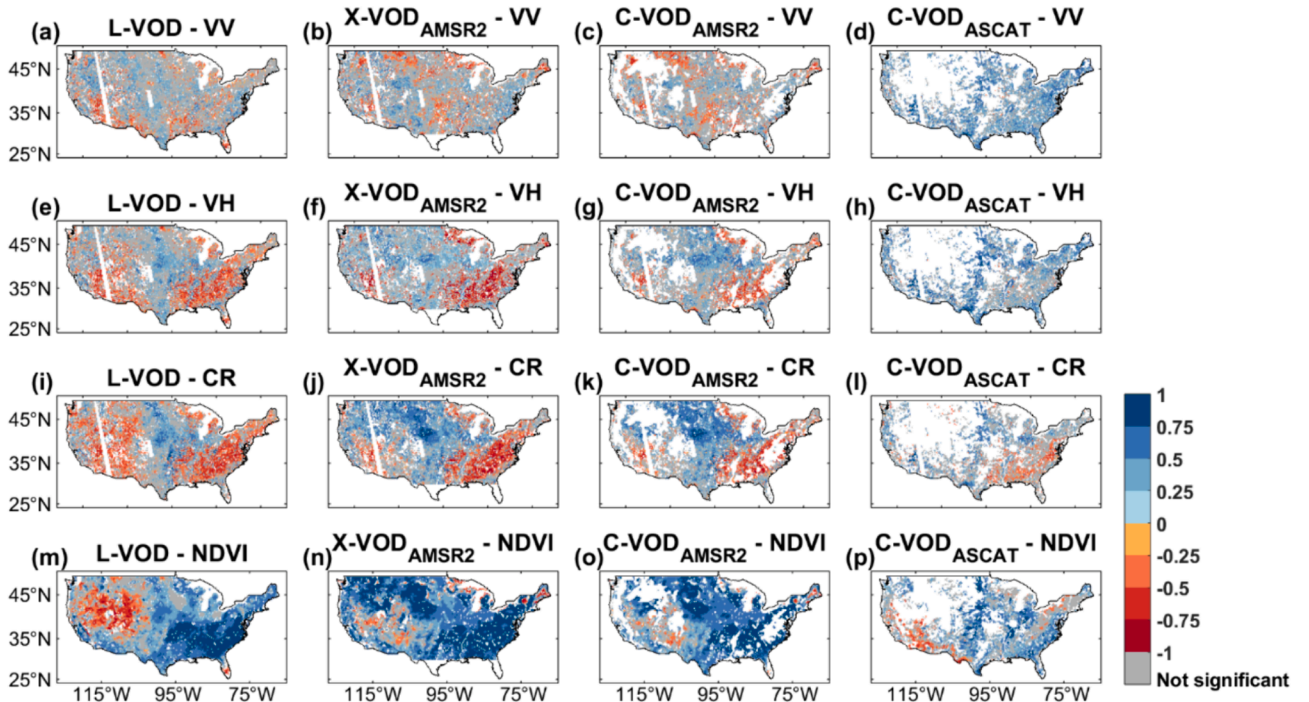


Fig. 5. Per-pixel temporal correlation (R) between 16-day average values of VODs and proxies from 2017 to 2020. Gray areas represent pixels with insignificant ($p > 0.05$) correlations. White pixels indicate “absence of valid data”.

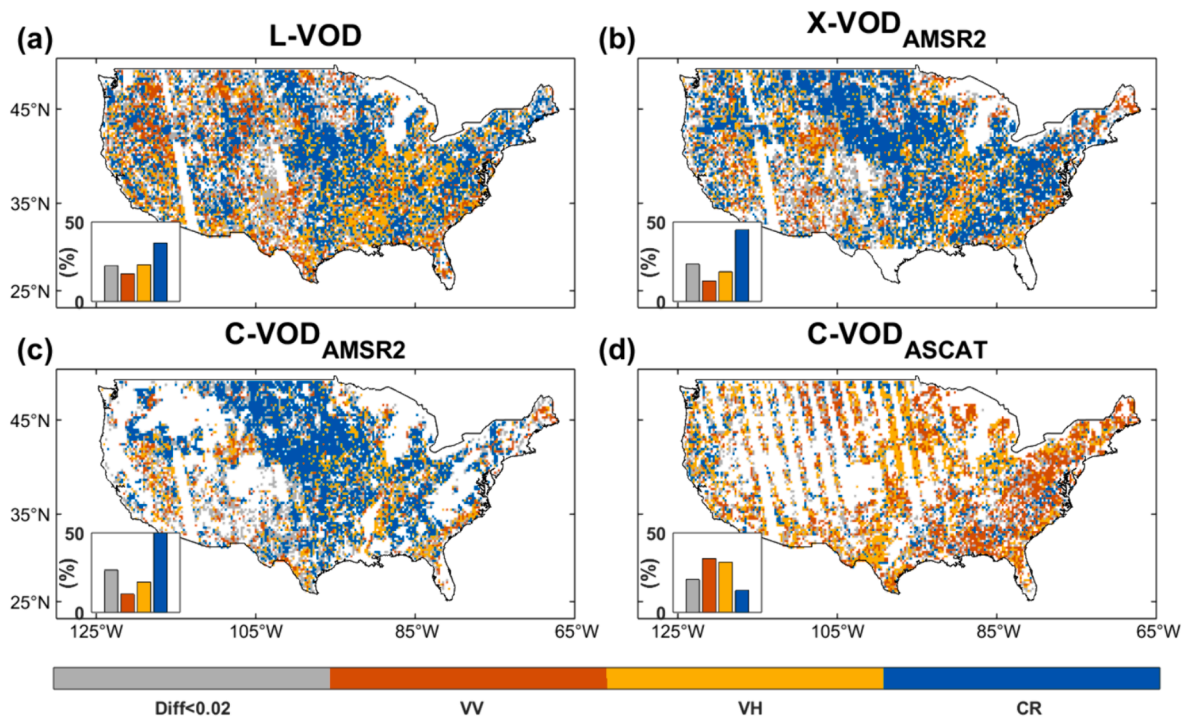


Fig. 6. Spatial distribution showing which active-microwave proxy (VV, VH, or CR) correlates most highly with VODs. (a) L-VOD, (b) X-VOD_{AMSR2}, (c) C-VOD_{AMSR2} and (d) C-VOD_{ASCAT}. Pixels with absolute values of R difference below 0.02 are indicated in gray. White pixels indicate “absence of valid data”.

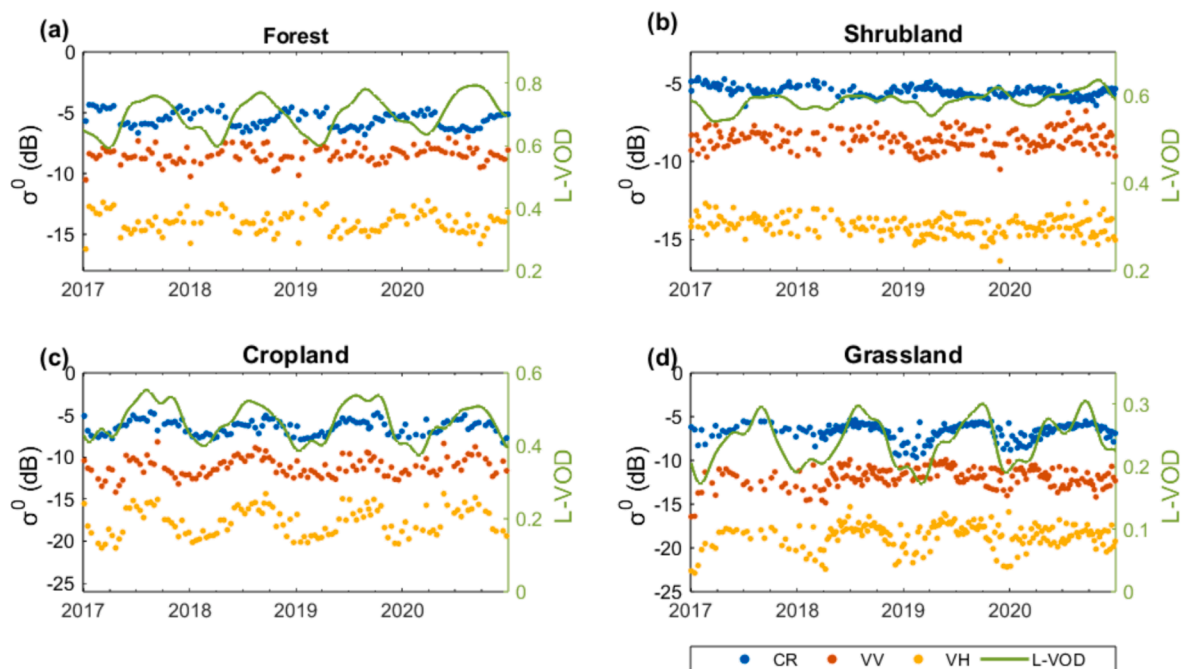


Fig. 7. Time series of Sentinel-1 CR (blue), VV (orange), VH (yellow) and L-VOD over the period 2017–2020 at 4 sites. Site details, including vegetation type and latitude/longitude: (a) forest, (38.38°N/81.88°W); (b) shrubland, (46.38°N/119.88°W); (c) cropland, (34.63°N/78.38°W); and (d) grassland, (35.88°N/97.13°W). The locations of these sites are shown in Fig. 1. (For interpretation of the references to colour in this figure legend, the reader is referred to the web version of this article.)

5.2. Performance of temporal correlations

In the forest area, high positive temporal correlations between VOD and NDVI could be observed, but the temporal correlations between VOD and active-microwave proxies were generally negative. The positive correlations between VOD and NDVI could be explained by that the

seasonal cycle mostly produces foliation/defoliation processes, particularly for the broadleaf deciduous forests of the southeastern U.S. VOD and NDVI are higher in full leaf development than in defoliated stage (Li et al., 2021). On the contrary, active-microwave proxies were negatively correlated with VOD, which could be attributed to the fact that VV- and VH-pol backscattering coefficients are lower in the leaf development

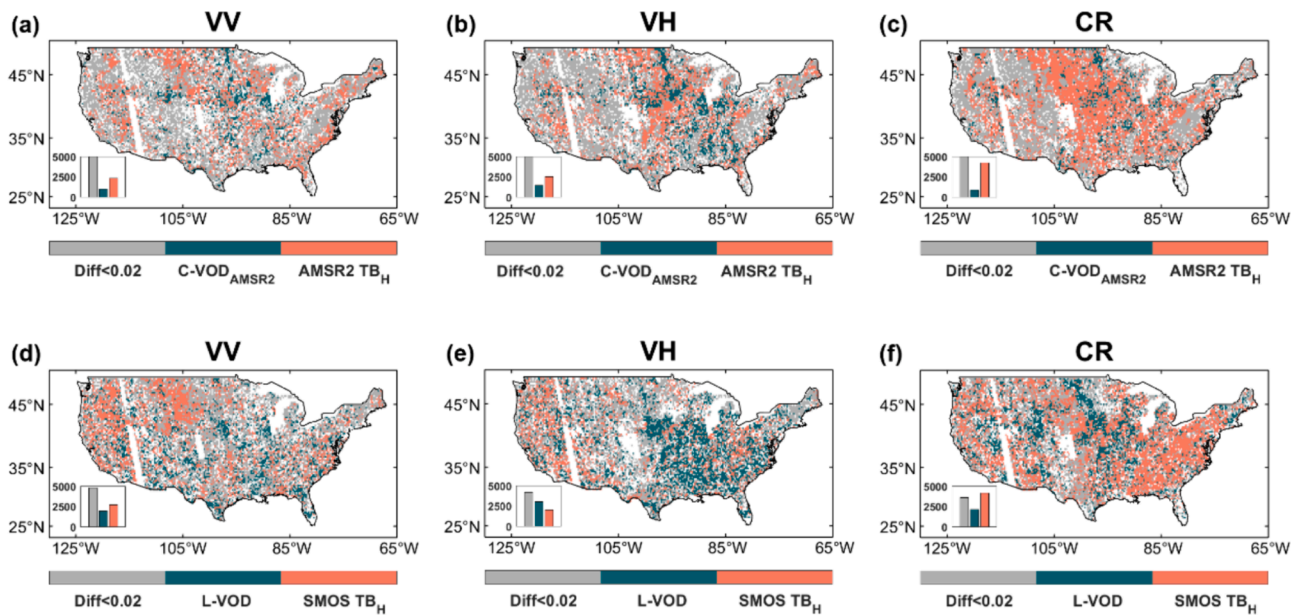


Fig. 8. Maps showing which dataset (VOD or TB_H) obtained the highest absolute temporal correlation (R) values with active-microwave proxies (VV, VH and CR), along with the corresponding number of pixels in the subplot (bottom left). Pixels with absolute values of R difference below 0.02 are indicated in gray. White pixels indicate “absence of valid data”.

stage than in defoliated stage (Fig. 7a), because leaves attenuate the backscattering of branches and this effect is not compensated by their own backscattering (Rüetschi et al., 2018; Soudani et al., 2021; Vreugdenhil et al., 2020).

Note that, compared with the timeseries of the backscattering coefficients (i.e., VH and VV) over forest, VOD from passive microwave (e.g., L-VOD) has the opposite correlation relative to that from the active microwave (e.g., C-VOD_{AMSR2}). At a given frequency and for a given vegetated surface there is supposed to be a unique VOD. Therefore, it remains to be further investigated which VOD, retrieved by active or passive techniques, is more reliable.

For shrubland area, the observed negative correlations between active-microwave proxies and VOD are more difficult to be explained. This negative correlation between NDVI and VOD was also reported by previous studies which found temporal lags within some environments between different climate and vegetation parameters (Jones et al., 2014; Tian et al., 2018). Specifically, in the Amazonian forests, it was found that the canopy biomass development phase (expressed by X-VOD) and net leaf flushing stage (expressed by LAI) were asynchronous (Jones et al., 2014). Similarly, Tian et al., (2018) discovered that in dry tropical woodlands, L-VOD lags behind the growth of leaves (expressed by LAI) as long as ~ 180 days, explaining the negative relationship between L-VOD and optical vegetation indices.

5.3. Implication for potential downscaling methods

The comparison of the correlations between coarse-resolution VOD and active-microwave proxies vs. the correlations between coarse-resolution TB datasets and active-microwave proxies provided the important implications for coarse-resolution VOD downscaling methods. Specifically, downscaling of coarse-resolution VOD products using high-resolution active-microwave proxies is supposed to be more prospective relative to disaggregating TB with those proxies, due to the poor spatial correlations between TB datasets and active-microwave proxies. Moreover, there were more highly correlated pixels between L-VOD and VH (2541 pixels, Fig. 8e), compared to the correlations between L-VOD and VV (Fig. 8d), suggesting that VH could perform better in downscaling coarse-resolution L-VOD relative to VV. Thus, using VH in the downscaling method could produce improvements with respect to

the existing methods, such as the one proposed by Bousquet et al., (2019), which disaggregated L-VOD at the spatial scale using VV-pol backscatter. Therefore, downscaling of coarse-resolution VOD products using high-resolution proxies such as VH in a spatio-temporal machine learning framework is promising.

Furthermore, the advantages of downscaling coarse-resolution VOD products using high-resolution proxies with respect to a direct use of high-resolution proxies to estimate vegetation properties should be emphasized. Previous studies (Tian et al., 2017; Vicente-Serrano et al., 2016; Zhu and Liu, 2015) have employed the direct use of high-resolution proxies to estimate vegetation properties, but these proxies were limited by the atmospheric effects (from optical indices) and the saturation (from both optical and active-microwave proxies) over dense-vegetated regions (Imhoff, 1995; Joshi et al., 2017; Loranty et al., 2018). In contrast, high-resolution VOD obtained from the downscaling method could potentially overcome the issues mentioned above, due to the advantages of passive microwave observations (being unaffected by atmospheric conditions and highly sensitive to high-density vegetation (Frappart et al., 2020; Rodríguez-Fernández et al., 2018)). Moreover, VOD can better present the dynamics of the VWC and biomass over forest (Teubner et al., 2018; Vittucci et al., 2019), which means that high-resolution VOD can provide alternative important information related to vegetation properties, relative to optical proxies (e.g., vegetation greenness indicated by NDVI).

5.4. Uncertainties

The revisit time of Sentinel-1 limited the correlation analysis with VODs over the contiguous U.S. In theory, Sentinel-1 is supposed to operate with a revisit cycle of 6 days with two sensors (A and B) in combination, but the acquisition frequency depends on different zones (Geudtner et al., 2014). Currently, for areas outside of Europe, the completeness of Sentinel-1's data coverage may limit the data availability. In the U.S., the repetition period of Sentinel-1 is 6 to 12 days and some of the orbital data are lacking. To avoid inconsistency in ascending/descending orbit data, the ascending orbit data of two sensors (A and B) was used in our study. However, this approach also reduces the data availability of Sentinel-1 in the study area, introducing uncertainty into the statistical results.

The correlation between NDVI and VOD could be affected by the quality of NDVI, because NDVI is contaminated by atmospheric conditions including aerosols scattering, water vapor absorption, and cloud cover, and its availability is reduced, as it is indicated by the lower observation frequency of NDVI (Fig. S12a) with respect to the one of active-microwave proxies (Fig. S12b).

The different overpass times of MODIS, Sentinel-1 and other microwave satellites could result in uncertainties in the calculation of the relationships between VODs and proxies, although the vegetation pattern was expected to persist spatially over several days. This assumption can be generally met, under the condition that no extreme climatic events occur associated with large vegetation losses over a short term (e.g., 7–15 days).

Besides, incidence angle diversity of Sentinel-1 needs to be taken into consideration to accurately estimate VOD in further downscaling work using the Sentinel-1 backscattering coefficients. The correlations between VOD products and backscattering coefficients collected at different local incidence angles could be limited by the angle effect. Normalized backscattering coefficients are able to improve the spatial correlation with VOD products (Table S2), e.g., the correlation coefficient between normalized VH and L-VOD (0.80) has improved by 0.02, relative to that between VH collected at different angles and L-VOD (0.78).

6. Conclusion

This study presented a quantitative assessment of the correlations between VOD products obtained at X-/C-/L-bands and Sentinel-1-based active-microwave proxies (VV, VH, and CR), as well as the MODIS optical vegetation index NDVI, in the perspective of downscaling the coarse-resolution VOD using high spatio-temporal resolution auxiliary proxies. In terms of spatial correlation, NDVI and VH had a high correlation with all four VOD products, with the highest spatial correlation between L-VOD and VH ($R = 0.80$), followed by L-VOD and NDVI ($R = 0.77$). In terms of per-pixel temporal correlation, NDVI and CR showed higher correlations with VOD, relative to VH and VV. Overall, NDVI correlated best with VOD products both spatially and temporally. However, it is necessary to integrate active-microwave proxies (VH and CR) as downscaling proxies, due to the limited temporal resolution of NDVI.

Although there are some uncertainties in our results due to the mismatch of revisit time between multi-source datasets and the saturation effects of active-microwave and optical indices, the assessments provide some crucial implications for retrieving high-resolution VOD. TB exhibited a comparable and even stronger temporal correlation with active-microwave proxies, relative to VOD, while its spatial correlations with such proxies were poor. Therefore, in a spatio-temporal machine learning framework, downscaling of coarse-resolution VOD products using high-resolution active-microwave proxies is supposed to be more promising relative to disaggregating TB with those proxies. Recently developed downscaling methods, e.g., machine learning (Mohite et al., 2022; Xu et al., 2020) or empirical radiative transfer model (Merlin et al., 2008), could be promising ways to accurately obtain high-resolution VOD by using the optimal proxies.

CRedit authorship contribution statement

Shiyu Zhong: Writing – original draft, Software, Methodology, Investigation, Data curation, Conceptualization. **Lei Fan:** Writing – review & editing, Supervision, Methodology, Funding acquisition, Data curation, Conceptualization. **Gabrielle De Lannoy:** Writing – review & editing, Methodology, Conceptualization. **Frédéric Frappart:** Writing – review & editing, Conceptualization. **Jiangyuan Zeng:** Writing – review & editing, Conceptualization. **Mariette Vreugdenhil:** Writing – review & editing, Methodology, Conceptualization. **Jian Peng:** Writing – review & editing. **Xiangzhuo Liu:** Writing – review & editing, Data

curation. **Zanpin Xing:** Writing – review & editing, Methodology. **Mengjia Wang:** Methodology, Data curation. **Xiaojun Li:** Methodology, Data curation. **Huan Wang:** Methodology. **Jean-Pierre Wigneron:** Writing – review & editing, Methodology.

Declaration of competing interest

The authors declare that they have no known competing financial interests or personal relationships that could have appeared to influence the work reported in this paper.

Data availability

Data will be made available on request.

Acknowledgement

This work was supported by National Natural Science Foundation of China (42171339, 42322103), and the special fund for youth team of Southwest University (SWU-XJLJ202305).

Appendix A. Supplementary data

Supplementary data to this article can be found online at <https://doi.org/10.1016/j.jag.2024.103910>.

References

- Al Bitar, A., Mialon, A., Kerr, Y.H., Cabot, F., Richaume, P., Jacquette, E., Quesney, A., Mahmoodi, A., Tarot, S., Parrens, M., Al-Yaari, A., Pellarin, T., Rodriguez-Fernandez, N., Wigneron, J.-P., 2017. The global SMOS Level 3 daily soil moisture and brightness temperature maps. *Earth Syst. Sci. Data* 9, 293–315. <https://doi.org/10.5194/essd-9-293-2017>.
- Attema, E.P.W., Ulaby, F.T., 1978. Vegetation modeled as a water cloud. *Radio Sci.* 13, 357–364. <https://doi.org/10.1029/RS013i002p00357>.
- Bauer-Marschallinger, B., Freeman, V., Cao, S., Paulik, C., Schauffer, S., Stachl, T., Modanesi, S., Massari, C., Ciabatta, L., Brocca, L., Wagner, W., 2019. Toward Global Soil Moisture Monitoring With Sentinel-1: Harnessing Assets and Overcoming Obstacles. *IEEE Trans. Geosci. Remote Sens.* 57, 520–539. <https://doi.org/10.1109/TGRS.2018.2858004>.
- Bousquet, E., Mialon, A., Rodriguez-Fernandez, N.J., Mermoz, S., Bouvet, A., Merlin, O., Kerr, Y.H., 2019. Combining L-Band Radar and Smos L-Band VOD for High Resolution Estimation of Biomass, in: IGARSS 2019 - 2019 IEEE International Geoscience and Remote Sensing Symposium. Presented at the IGARSS 2019 - 2019 IEEE International Geoscience and Remote Sensing Symposium, IEEE, Yokohama, Japan, pp. 5508–5511. doi: 10.1109/IGARSS.2019.8899268.
- Brandt, M., Wigneron, J.-P., Chave, J., Tagesson, T., Penuelas, J., Ciais, P., Rasmussen, K., Tian, F., Mbow, C., Al-Yaari, A., Rodriguez-Fernandez, N., Schurgers, G., Zhang, W., Chang, J., Kerr, Y., Verger, A., Tucker, C., Mialon, A., Rasmussen, L.V., Fan, L., Fensholt, R., 2018. Satellite passive microwaves reveal recent climate-induced carbon losses in African drylands. *Nat. Ecol. Evol.* 2, 827–835. <https://doi.org/10.1038/s41559-018-0530-6>.
- Chaparro, D., Duveiller, G., Piles, M., Cescatti, A., Vall-llossera, M., Camps, A., Entekhabi, D., 2019. Sensitivity of L-band vegetation optical depth to carbon stocks in tropical forests: a comparison to higher frequencies and optical indices. *Remote Sens. Environ.* 232, 111303 <https://doi.org/10.1016/j.rse.2019.111303>.
- Chaubell, J., Yueh, S., Dunbar, R.S., Colliander, A., Entekhabi, D., Chan, S.K., Chen, F., Xu, X., Bindlish, R., O'Neill, P., Asanuma, J., Berg, A.A., Bosch, D.D., Caldwell, T., Cosh, M.H., Collins, C.H., Jensen, K.H., Martínez-Fernández, J., Seyfried, M., Starks, P.J., Su, Z., Thibeault, M., Walker, J.P., 2022. Regularized Dual-Channel Algorithm for the Retrieval of Soil Moisture and Vegetation Optical Depth From SMAP Measurements. *IEEE J. Sel. Top. Appl. Earth Obs. Remote Sens.* 15, 102–114. <https://doi.org/10.1109/JSTARS.2021.3123932>.
- Cui, T., Fan, L., Ciais, P., Fensholt, R., Frappart, F., Sitch, S., Chave, J., Chang, Z., Li, X., Wang, M., Liu, X., Ma, M., Wigneron, J.-P., 2023. First assessment of optical and microwave remotely sensed vegetation proxies in monitoring aboveground carbon in tropical Asia. *Remote Sens. Environ.* 293, 113619 <https://doi.org/10.1016/j.rse.2023.113619>.
- Das, N.N., Entekhabi, D., Njoku, E.G., Shi, J.J.C., Johnson, J.T., Colliander, A., 2014. Tests of the SMAP Combined Radar and Radiometer Algorithm Using Airborne Field Campaign Observations and Simulated Data. *IEEE Trans. Geosci. Remote Sens.* 52, 2018–2028. <https://doi.org/10.1109/TGRS.2013.2257605>.
- Das, N.N., Entekhabi, D., Dunbar, R.S., Chaubell, M.J., Colliander, A., Yueh, S., Jagdhuber, T., Chen, F., Crow, W., O'Neill, P.E., Walker, J.P., Berg, A., Bosch, D.D., Caldwell, T., Cosh, M.H., Collins, C.H., Lopez-Baeza, E., Thibeault, M., 2019. The SMAP and Copernicus Sentinel 1A/B microwave active-passive high resolution

- surface soil moisture product. *Remote Sens. Environ.* 233, 111380 <https://doi.org/10.1016/j.rse.2019.111380>.
- Didan, K., 2015. MODIS 3A3 MODIS/Terra Vegetation Indices Monthly L3 Global 1km SIN Grid V006. doi: 10.5067/MODIS/MODIS3A3.006.
- El Hajj, M., Baghdadi, N., Wigneron, J.-P., Zribi, M., Albergel, C., Calvet, J.-C., Fayad, I., 2019. First Vegetation Optical Depth Mapping from Sentinel-1 C-band SAR Data over Crop Fields. *Remote Sens.* 11, 2769. <https://doi.org/10.3390/rs11232769>.
- ESA. Land Cover CCI Product User Guide Version 2. Tech. Rep. (2017). Available at: maps.elie.ucl.ac.be/CCI/viewer/download/ESACCI-LC-Ph2-PUGv2.2.0.pdf.
- Fan, L., Wigneron, J.-P., Ciais, P., Chave, J., Brandt, M., Fensholt, R., Saatchi, S.S., Bastos, A., Al-Yaari, A., Hufkens, K., Qin, Y., Xiao, X., Chen, C., Myneni, R.B., Fernandez-Moran, R., Mialon, A., Rodriguez-Fernandez, N.J., Kerr, Y., Tian, F., Peñuelas, J., 2019. Satellite-Observed Pantropical Carbon Dynamics. *Nat. Plants* 5, 944–951. <https://doi.org/10.1038/s41477-019-0478-9>.
- Fan, L., Xing, Z., Lannoy, G.D., Frappart, F., Peng, J., Zeng, J., Li, X., Yang, K., Zhao, T., Shi, J., Ma, H., Wang, M., Liu, X., Yi, C., Ma, M., Tang, X., Wen, J., Chen, X., Wang, C., Wang, L., Wang, G., Wigneron, J.-P., 2022. Evaluation of satellite and reanalysis estimates of surface and root-zone soil moisture in croplands of Jiangsu Province, China. *Remote Sens. Environ.* 282, 113283 <https://doi.org/10.1016/j.rse.2022.113283>.
- Fan, L., Wigneron, J.-P., Ciais, P., Chave, J., Brandt, M., Sitch, S., Yue, C., Bastos, A., Li, X., Qin, Y., Yuan, W., Schepaschenko, D., Mukhortova, L., Li, X., Liu, X., Wang, M., Frappart, F., Xiao, X., Chen, J., Ma, M., Wen, J., Chen, X., Yang, H., van Wees, D., Fensholt, R., 2023. Siberian carbon sink reduced by forest disturbances. *Nat. Geosci.* 16, 56–62. <https://doi.org/10.1038/s41561-022-01087-x>.
- Filipponi, F., 2019. Sentinel-1 GRD Preprocessing Workflow. *Proceedings* 18, 11. doi: 10.3390/ECRS-3-06201.
- Frappart, F., Wigneron, J.-P., Li, X., Liu, X., Al-Yaari, A., Fan, L., Wang, M., Moisy, C., Le Masson, E., Aoulad Lafkhi, Z., Vallé, C., Ygorra, B., Baghdadi, N., 2020. Global Monitoring of the Vegetation Dynamics from the Vegetation Optical Depth (VOD): A Review. *Remote Sens.* 12, 2915. <https://doi.org/10.3390/rs12182915>.
- Geudtner, D., Torres, R., Snoei, P., Davidson, M., Rommen, B., 2014. Sentinel-1 System capabilities and applications, in: 2014 IEEE Geoscience and Remote Sensing Symposium. Presented at the 2014 IEEE Geoscience and Remote Sensing Symposium, pp. 1457–1460. doi: 10.1109/IGARSS.2014.6946711.
- Hauke, J., Kosowski, T., 2011. Comparison of Values of Pearson's and Spearman's Correlation Coefficients on the Same Sets of Data. *QUA GEO* 30, 87–93. <https://doi.org/10.2478/v10117-011-0021-1>.
- Imhoff, M.L., 1995. Radar backscatter and biomass saturation: ramifications for global biomass inventory. *IEEE Trans. Geosci. Remote Sens.* 33, 511–518. <https://doi.org/10.1109/TGRS.1995.8746034>.
- Jackson, T.J., Schmugge, T.J., 1991. Vegetation effects on the microwave emission of soils. *Remote Sens. Environ.* 36, 203–212. [https://doi.org/10.1016/0034-4257\(91\)90057-D](https://doi.org/10.1016/0034-4257(91)90057-D).
- Jiao, X., McNairn, H., Shang, J., Pattey, E., Liu, J., Champagne, C., 2009. The sensitivity of RADARSAT-2 quad-polarization SAR data to crop LAI, in: *Remote Sensing and Modeling of Ecosystems for Sustainability VI*. Presented at the Remote Sensing and Modeling of Ecosystems for Sustainability VI, SPIE, pp. 136–146. doi: 10.1117/12.825701.
- Jones, M.O., Kimball, J.S., Nemani, R.R., 2014. Asynchronous Amazon forest canopy phenology indicates adaptation to both water and light availability. *Environ. Res. Lett.* 9, 124021 <https://doi.org/10.1088/1748-9326/9/12/124021>.
- Joshi, N., Mitchard, E.T.A., Broll, M., Schumacher, J., Fernández-Landa, A., Johannsen, V.K., Marchamalo, M., Fensholt, R., 2017. Understanding 'saturation' of radar signals over forests. *Sci. Rep.* 7, 3505. <https://doi.org/10.1038/s41598-017-03469-3>.
- Karthikeyan, L., Pan, M., Konings, A.G., Piles, M., Fernandez-Moran, R., Nagesh Kumar, D., Wood, E.F., 2019. Simultaneous retrieval of global scale Vegetation Optical Depth, surface roughness, and soil moisture using X-band AMSR-E observations. *Remote Sens. Environ.* 234, 111473 <https://doi.org/10.1016/j.rse.2019.111473>.
- Khabbazan, S., Steele-Dunne, S.C., Vermunt, P., Judge, J., Vreugdenhil, M., Gao, G., 2022. The influence of surface canopy water on the relationship between L-band backscatter and biophysical variables in agricultural monitoring. *Remote Sens. Environ.* 268, 112789 <https://doi.org/10.1016/j.rse.2021.112789>.
- Kim, Y., Jackson, T., Bindlish, R., Lee, H., Hong, S., 2012. Radar Vegetation Index for Estimating the Vegetation Water Content of Rice and Soybean. *IEEE Geosci. Remote Sens. Lett.* 9, 564–568. <https://doi.org/10.1109/LGRS.2011.2174772>.
- Konings, A.G., Piles, M., Rötter, K., McColl, K.A., Chan, S.K., Entekhabi, D., 2016. Vegetation optical depth and scattering albedo retrieval using time series of dual-polarized L-band radiometer observations. *Remote Sens. Environ.* 172, 178–189. <https://doi.org/10.1016/j.rse.2015.11.009>.
- Lawrence, H., Wigneron, J.-P., Richaume, P., Novello, N., Grant, J., Mialon, A., Al Bitar, A., Merlin, O., Guyon, D., Leroux, D., Bircher, S., Kerr, Y., 2014. Comparison between SMOS Vegetation Optical Depth products and MODIS vegetation indices over crop zones of the USA. *Remote Sens. Environ.* 140, 396–406. <https://doi.org/10.1016/j.rse.2013.07.021>.
- Li, X., Wigneron, J.-P., Frappart, F., Fan, L., Ciais, P., Fensholt, R., Entekhabi, D., Brandt, M., Konings, A.G., Liu, X., Wang, M., Al-Yaari, A., Moisy, C., 2021. Global-scale assessment and inter-comparison of recently developed/reprocessed microwave satellite vegetation optical depth products. *Remote Sens. Environ.* 253, 112208 <https://doi.org/10.1016/j.rse.2020.112208>.
- Li, X., Wigneron, J.-P., Frappart, F., Lannoy, G.D., Fan, L., Zhao, T., Gao, L., Tao, S., Ma, H., Peng, Z., Liu, X., Wang, H., Wang, M., Moisy, C., Ciais, P., 2022. The first global soil moisture and vegetation optical depth product retrieved from fused SMOS and SMAP L-band observations. *Remote Sens. Environ.* 282, 113272 <https://doi.org/10.1016/j.rse.2022.113272>.
- Liu, Y.Y., van Dijk, A.I.J.M., Miralles, D.G., McCabe, M.F., Evans, J.P., de Jeu, R.A.M., Gentile, P., Huete, A., Parinussa, R.M., Wang, L., Guan, K., Berry, J., Restrepo-Coupe, N., 2018. Enhanced canopy growth precedes senescence in 2005 and 2010 Amazonian droughts. *Remote Sens. Environ.* 211, 26–37. <https://doi.org/10.1016/j.rse.2018.03.035>.
- Liu, X., Wigneron, J.-P., Fan, L., Frappart, F., Ciais, P., Baghdadi, N., Zribi, M., Jagdhuber, T., Li, X., Wang, M., Bai, X., Moisy, C., 2021. ASCAT IB: A radar-based vegetation optical depth retrieved from the ASCAT scatterometer satellite. *Remote Sens. Environ.* 264, 112587 <https://doi.org/10.1016/j.rse.2021.112587>.
- Liu, X., Wigneron, J.-P., Wagner, W., Frappart, F., Fan, L., Vreugdenhil, M., Baghdadi, N., Zribi, M., Jagdhuber, T., Tao, S., Li, X., Wang, H., Wang, M., Bai, X., Mousa, B.G., Ciais, P., 2023. A new global C-band vegetation optical depth product from ASCAT: Description, evaluation, and inter-comparison. *Remote Sens. Environ.* 299, 113850 <https://doi.org/10.1016/j.rse.2023.113850>.
- Lorant, M.M., Davydov, S.P., Kropp, H., Alexander, H.D., Mack, M.C., Natali, S.M., Zimov, N.S., 2018. Vegetation Indices Do Not Capture Forest Cover Variation in Upland Siberian Larch Forests. *Remote Sens.* 10, 1686. <https://doi.org/10.3390/rs10111686>.
- Lucas, R.M., Cronin, N., Lee, A., Moghaddam, M., Witte, C., Tickle, P., 2006. Empirical relationships between AIRSAR backscatter and Lidar-derived forest biomass, Queensland, Australia. *Remote Sens. Environ.* 100, 407–425. <https://doi.org/10.1016/j.rse.2005.10.019>.
- McNairn, H., Shang, J., 2016. A Review of Multitemporal Synthetic Aperture Radar (SAR) for Crop Monitoring. In: Ban, Y. (Ed.), *Multitemporal Remote Sensing: Methods and Applications*, Remote Sensing and Digital Image Processing. Springer International Publishing, Cham, pp. 317–340. https://doi.org/10.1007/978-3-319-47037-5_15.
- Merlin, O., Walker, J.P., Chehbouni, A., Kerr, Y., 2008. Towards deterministic downscaling of SMOS soil moisture using MODIS derived soil evaporative efficiency. *Remote Sens. Environ.* 112, 3935–3946. <https://doi.org/10.1016/j.rse.2008.06.012>.
- Moisinger, L., Dorigo, W., de Jeu, R., van der Schalie, R., Scanlon, T., Teubner, I., Forkel, M., 2020. The global long-term microwave Vegetation Optical Depth Climate Archive (VODCA). *Earth Syst. Sci. Data* 12, 177–196. <https://doi.org/10.5194/essd-12-177-2020>.
- Mohite, J., Sawant, S., Pandit, A., Pappula, S., 2022. Spatial Downscaling of Vegetation Optical Depth Using the Modis and Srtm Observations. In: *IGARSS 2022–2022 IEEE International Geoscience and Remote Sensing Symposium*. Presented at the IGARSS 2022–2022 IEEE International Geoscience and Remote Sensing Symposium, pp. 5870–5873. <https://doi.org/10.1109/IGARSS46834.2022.9884507>.
- Momen, M., Wood, J.D., Novick, K.A., Pangle, R., Pockman, W.T., McDowell, N.G., Konings, A.G., 2017. Interacting Effects of Leaf Water Potential and Biomass on Vegetation Optical Depth. *J. Geophys. Res. Biogeosciences* 122, 3031–3046. <https://doi.org/10.1002/2017JG004145>.
- Olivares-Cabello, C., Chaparro, D., Vall-llossera, M., Camps, A., López-Martínez, C., 2023. Global Unsupervised Assessment of Multifrequency Vegetation Optical Depth Sensitivity to Vegetation Cover. *IEEE J. Sel. Top. Appl. Earth Obs. Remote Sens.* 16, 538–552. <https://doi.org/10.1109/JSTARS.2022.3226001>.
- Owe, M., de Jeu, R., Walker, J., 2001. A methodology for surface soil moisture and vegetation optical depth retrieval using the microwave polarization difference index. *IEEE Trans. Geosci. Remote Sens.* 39, 1643–1654. <https://doi.org/10.1109/36.942542>.
- Owe, M., de Jeu, R., Holmes, T., 2008. Multisensor historical climatology of satellite-derived global land surface moisture. *J. Geophys. Res. Earth Surf.* 113 <https://doi.org/10.1029/2007JF000769>.
- Peng, J., Loew, A., Merlin, O., Verhoest, N.E.C., 2017. A review of spatial downscaling of satellite remotely sensed soil moisture. *Rev. Geophys.* 55, 341–366. <https://doi.org/10.1002/2016RG000543>.
- Rodríguez-Fernández, N.J., Mialon, A., Mermoz, S., Bouvet, A., Richaume, P., Al Bitar, A., Al-Yaari, A., Brandt, M., Kaminski, T., Le Toan, T., Kerr, Y.H., Wigneron, J.-P., 2018. An evaluation of SMOS L-band vegetation optical depth (L-VOD) data sets: high sensitivity of L-VOD to above-ground biomass in Africa. *Biogeosciences* 15, 4627–4645. <https://doi.org/10.5194/bg-15-4627-2018>.
- Rötter, K., Montzka, C., Entekhabi, D., Konings, A.G., McColl, K.A., Piles, M., Vereecken, H., 2017. Relationship Between Vegetation Microwave Optical Depth and Cross-Polarized Backscatter From Multiyear Aquarius Observations. *IEEE J. Sel. Top. Appl. Earth Obs. Remote Sens.* 10, 4493–4503. <https://doi.org/10.1109/JSTARS.2017.2716638>.
- Rüetschi, M., Schaepman, M.E., Small, D., 2018. Using Multitemporal Sentinel-1 C-band Backscatter to Monitor Phenology and Classify Deciduous and Coniferous Forests in Northern Switzerland. *Remote Sens.* 10, 55. <https://doi.org/10.3390/rs10010055>.
- Schmidt, L., Forkel, M., Zotta, R.-M., Scherrer, S., Dorigo, W.A., Kuhn-Régner, A., van der Schalie, R., Yebra, M., 2023. Assessing the sensitivity of multi-frequency passive microwave vegetation optical depth to vegetation properties. *Biogeosciences* 20, 1027–1046. <https://doi.org/10.5194/bg-20-1027-2023>.
- Soudani, K., Delpierre, N., Berveiller, D., Hmimina, G., Vincent, G., Morfin, A., Dufrene, E., 2021. Potential of C-band Synthetic Aperture Radar Sentinel-1 time-series for the monitoring of phenological cycles in a deciduous forest. *Int. J. Appl. Earth Obs. Geoinformation* 104, 102505. <https://doi.org/10.1016/j.jag.2021.102505>.
- Teubner, I.E., Forkel, M., Jung, M., Liu, Y.Y., Miralles, D.G., Parinussa, R., van der Schalie, R., Vreugdenhil, M., Schwalm, C.R., Tramontana, G., Camps-Valls, G., Dorigo, W.A., 2018. Assessing the relationship between microwave vegetation optical depth and gross primary production. *Int. J. Appl. Earth Obs. Geoinformation* 65, 79–91. <https://doi.org/10.1016/j.jag.2017.10.006>.

- Tian, J., Wang, L., Li, X., Gong, H., Shi, C., Zhong, R., Liu, X., 2017. Comparison of UAV and WorldView-2 imagery for mapping leaf area index of mangrove forest. *Int. J. Appl. Earth Obs. Geoinformation* 61, 22–31. <https://doi.org/10.1016/j.jag.2017.05.002>.
- Tian, F., Wigneron, J.-P., Ciais, P., Chave, J., Ogée, J., Peñuelas, J., Ræbild, A., Domec, J.-C., Tong, X., Brandt, M., Mialon, A., Rodríguez-Fernandez, N., Tagessson, T., Al-Yaari, A., Kerr, Y., Chen, C., Myneni, R.B., Zhang, W., Ardö, J., Fensholt, R., 2018. Coupling of ecosystem-scale plant water storage and leaf phenology observed by satellite. *Nat. Ecol. Evol.* 2, 1428–1435. <https://doi.org/10.1038/s41559-018-0630-3>.
- Tong, X., Brandt, M., Yue, Y., Ciais, P., Rudbeck Jepsen, M., Penuelas, J., Wigneron, J.-P., Xiao, X., Song, X.-P., Horion, S., Rasmussen, K., Saatchi, S., Fan, L., Wang, K., Zhang, B., Chen, Z., Wang, Y., Li, X., Fensholt, R., 2020. Forest management in southern China generates short term extensive carbon sequestration. *Nat. Commun.* 11, 129. <https://doi.org/10.1038/s41467-019-13798-8>.
- Torres, R., Snoeijs, P., Geudtner, D., Bibby, D., Davidson, M., Attema, E., Potin, P., Rommen, B., Floury, N., Brown, M., Traver, I.N., Deghaye, P., Duesmann, B., Rosich, B., Miranda, N., Bruno, C., L'Abbate, M., Croci, R., Pietropaolo, A., Huchler, M., Rostan, F., 2012. GMES Sentinel-1 mission. *Remote Sens. Environ.* 120, 9–24. <https://doi.org/10.1016/j.rse.2011.05.028>.
- Ulaby, F.T., Moore, R.K., Fung, A.K., 1982. Microwave remote sensing: Active and passive. Volume 2 - Radar remote sensing and surface scattering and emission theory.
- Vachaud, G., Passerat De Silans, A., Balabanis, P., Vauclin, M., 1985. Temporal Stability of Spatially Measured Soil Water Probability Density Function. *Soil Sci. Soc. Am. J.* 49, 822–828. <https://doi.org/10.2136/sssaj1985.03615995004900040006x>.
- Veloso, A., Mermoz, S., Bouvet, A., Le Toan, T., Planells, M., Dejoux, J.-F., Ceschia, E., 2017. Understanding the temporal behavior of crops using Sentinel-1 and Sentinel-2-like data for agricultural applications. *Remote Sens. Environ.* 199, 415–426. <https://doi.org/10.1016/j.rse.2017.07.015>.
- Vicente-Serrano, S.M., Camarero, J.J., Olano, J.M., Martín-Hernández, N., Peña-Gallardo, M., Tomás-Burguera, M., Gazol, A., Azorin-Molina, C., Bhuyan, U., El Kenawy, A., 2016. Diverse relationships between forest growth and the Normalized Difference Vegetation Index at a global scale. *Remote Sens. Environ.* 187, 14–29. <https://doi.org/10.1016/j.rse.2016.10.001>.
- Vittucci, C., Vaglio Laurin, G., Tramontana, G., Ferrazzoli, P., Guerriero, L., Papale, D., 2019. Vegetation optical depth at L-band and above ground biomass in the tropical range: Evaluating their relationships at continental and regional scales. *Int. J. Appl. Earth Obs. Geoinformation* 77, 151–161. <https://doi.org/10.1016/j.jag.2019.01.006>.
- Vreugdenhil, M., Wagner, W., Bauer-Marschallinger, B., Pfeil, I., Teubner, I., Rüdiger, C., Strauss, P., 2018. Sensitivity of Sentinel-1 Backscatter to Vegetation Dynamics: An Austrian Case Study. *Remote Sens.* 10, 1396. <https://doi.org/10.3390/rs10091396>.
- Vreugdenhil, M., Navacchi, C., Bauer-Marschallinger, B., Hahn, S., Steele-Dunne, S., Pfeil, I., Dorigo, W., Wagner, W., 2020. Sentinel-1 Cross Ratio and Vegetation Optical Depth: A Comparison over Europe. *Remote Sens.* 12, 3404. <https://doi.org/10.3390/rs12203404>.
- Wagner, W., Hahn, S., Kidd, R., Melzer, T., Bartalis, Z., Hasenauer, S., Figa-Saldaña, J., de Rosnay, P., Jann, A., Schneider, S., Komma, J., Kubu, G., Brugger, K., Aubrecht, C., Züger, J., Gangkofner, U., Kienberger, S., Brocca, L., Wang, Y., Blöschl, G., Eitzinger, J., Steinnocher, K., 2013. The ASCAT Soil Moisture Product: A Review of its Specifications, Validation Results, and Emerging Applications. *Meteorol. z.* 5–33. <https://doi.org/10.1127/0941-2948/2013/0399>.
- Wang, M., Fan, L., Frappart, F., Ciais, P., Sun, R., Liu, Y., Li, X., Liu, X., Moisy, C., Wigneron, J.-P., 2021a. An alternative AMSR2 vegetation optical depth for monitoring vegetation at large scales. *Remote Sens. Environ.* 263, 112556. <https://doi.org/10.1016/j.rse.2021.112556>.
- Wang, M., Wigneron, J.-P., Sun, R., Fan, L., Frappart, F., Tao, S., Chai, L., Li, X., Liu, X., Ma, H., Moisy, C., Ciais, P., 2021b. A consistent record of vegetation optical depth retrieved from the AMSR-E and AMSR2 X-band observations. *Int. J. Appl. Earth Obs. Geoinformation* 105, 102609. <https://doi.org/10.1016/j.jag.2021.102609>.
- Wigneron, J.-P., Li, X., Frappart, F., Fan, L., Al-Yaari, A., De Lannoy, G., Liu, X., Wang, M., Le Masson, E., Moisy, C., 2021. SMOS-IC data record of soil moisture and L-VOD: Historical development, applications and perspectives. *Remote Sens. Environ.* 254, 112238. <https://doi.org/10.1016/j.rse.2020.112238>.
- Xu, Y., Wang, L., Ma, Z., Li, B., Bartels, R., Liu, C., Zhang, X., Dong, J., 2020. Spatially Explicit Model for Statistical Downscaling of Satellite Passive Microwave Soil Moisture. *IEEE Trans. Geosci. Remote Sens.* 58, 1182–1191. <https://doi.org/10.1109/TGRS.2019.2944421>.
- Zhou, Z., Fan, L., De Lannoy, G., Liu, X., Peng, J., Bai, X., Frappart, F., Baghdadi, N., Xing, Z., Li, X., Ma, M., Li, X., Che, T., Geng, L., Wigneron, J.-P., 2022. Retrieval of High-Resolution Vegetation Optical Depth from Sentinel-1 Data over a Grassland Region in the Heihe River Basin. *Remote Sens.* 14, 5468. <https://doi.org/10.3390/rs14215468>.
- Zhu, X., Liu, D., 2015. Improving forest aboveground biomass estimation using seasonal Landsat NDVI time-series. *ISPRS J. Photogramm. Remote Sens.* 102, 222–231. <https://doi.org/10.1016/j.isprsjprs.2014.08.014>.